A Multisensor Approach to Sea Ice Classification for the Validation of DMSP-SSM/I Passive Microwave Derived Sea Ice Products

K. Steffen
Department of Geography, Swiss Federal Institute of Technology, Winterthurerstrasse 190, CH-8057 Zürich, Switzerland
A. J. Schweiger
Cooperative Institute for Research in Environmental Sciences, University of Colorado, Campus Box 449, Boulder, CO 80309

ABSTRACT: The validation of sea ice products derived from the Special Sensor Microwave Imager (SSM/I) on board a DMSP platform is examined using data from the Landsat MSS and NOAA-AVHRR sensors. Image processing techniques for retrieving ice concentrations from each type of imagery are developed and results are intercompared to determine the ice parameter retrieval accuracy of the SSM/I NASA-Team algorithm. For case studies in the Beaufort Sea and East Greenland Sea, average retrieval errors of the SSM/I algorithm are between 1.7 percent for spring conditions and 4.3 percent during freeze up in comparison with Landsat derived ice concentrations. For a case study in the East Greenland Sea, SSM/I derived ice concentration in comparison with AVHRR imagery display a mean error of 9.6 percent.

INTRODUCTION

LONG-TERM MONITORING OF SEA ICE is of prime interest for studies of global climate. Polar oceans and their ice cover are more than passive indicators of change in global climate. They play an important role due to high-latitude air-ice-ocean interactions. Recent model results of Hansen *et al.* (1988) suggest that global greenhouse warming will soon rise above the level of natural climate variability. Model calculations predict this warming to occur most prominently around Antarctica and in the Arctic, where sea ice provides a positive climate feedback. It is thus of great importance to determine the accuracy with which sea ice parameters such as ice concentration and ice extent can be monitored with today's satellite technology.

Passive microwave data collected by satellites have been used to monitor sea ice in polar regions since 1973. Using the multiple frequencies provided by the Nimbus 7 Scanning Multichannel Microwave Radiometer (SMMR), 1978 to 1987, algorithms with the ability to derive sea ice concentrations have been developed (Cavalieri *et al.*, 1984; Comiso, 1986; Gloersen and Cavalieri, 1986; Steffen and Maslanik, 1988). On 19 June 1987 the Defense Meterological Satellite Program (DMSP) launched the Special Sensor Microwave Imager (SSM/I). The SSM/I is a passive microwave radiometer which provides near real-time data for operational use and for specific research areas (e.g., sea ice). This paper describes the validation of algorithms for determination of sea ice parameters which have been developed by NASA scientists (refered to as NASA-team algorithm) for the DMSP-SSM/I data stream. Our objective is to demonstrate a quantitative relationship between the SSM/I-derived sea ice parameters and those same parameters derived from other data sets, including visible and infrared satellite imagery. The general question to be addressed is with what accuracy (relative to these other observations) can we determine the following sea ice parameters: (1) position of the sea ice boundary, (2) total sea ice concentration, and (3) multi-year sea ice concentration.

In order to complete the analysis of DMSP SSM/I passive microwave sea ice products, several satellite data sets had to be merged. In the following section the techniques for the analysis of merged multisensor imagery from Landsat MSS (visible), AVHRR (visible and thermal infrared), and SSM/I (passive microwave) are presented.

DATA SETS AND METHODOLOGY

Several intercomparison case studies were carried out during the SSM/I validation period. For each case study we have assembled as much quantitative sea ice information (e.g., percent of ice concentration) as possible from two different satellites (Landsat MSS, NOAA AVHRR) and compared it to SSM/I derived sea ice products. The case studies were chosen to reflect the regional and temporal variability of the radiometric properties of sea ice. The comparison of Landsat and SSM/I derived ice concentrations mainly serves the purpose of determining the NASA-team algorithm accuracy and the influence of ice type distributions under cloud free condition at the smaller scale. The validation of SSM/I algorithm results using AVHRR imagery addresses the problem at a larger scale with particular attention to the influence of weather effects. Aerial photographic and high resolution microwave imagery corresponding to several satellite images was available and aides in their interpretation.

LANDSAT MSS

Cloud-free Landsat imagery was acquired for a range of ice conditions and geographic locations to allow for a validation of the SSM/I sea ice algorithm for a variety of ice concentrations and ice types. Landsat imagery was acquired in two formats: Landsat MSS digital imagery and Landsat MSS photographic transparencies.

Digital imagery. Geometrically and radiometrically corrected Landsat MSS imagery at 80-m resolution (field of view) is available from EOSAT corporation on computer compatible tape (CCT). This imagery can easily be georeferenced using ancillary header information and regridded to match the SSM/I grid format (polar stereographic projection). Due to the high reflectance levels of ice, MSS channels 4 to 6 are frequently saturated and can only be utilized in the ice parameter classification under low sun angle illumination conditions. However, reflectance differences between thin ice types and open water are greatest in the near infrared spectral range, so that MSS channel 7 (0.8 to 1.1 μm) is most suitable for the determination of ice concentrations.

Photographic transparencies. Due to data communication problems with the satellite downlink (TDRS), no digital imagery is available for some areas in the Bering, Chukchi, and Beaufort seas, but photographic transparencies were available through

PHOTOGRAMMETRIC ENGINEERING AND REMOTE SENSING,
Vol. 56, No. 1, January 1990, pp. 75–82.

0099-1112/90/5601–75$02.25/0

the Alaskan Quicklook system operated by the University of Alaska's Geophysical Institute (Miller *et al.*, 1981). This imagery is received in real time and recorded on photographic transparencies. Data are geometrically corrected for Earth rotation, but the frame centerpoint geolocation is unreliable due to the lack of accurate ephemeris and satellite attitude data. Landsat MSS channel 7 data were therefore acquired in swaths so that at least one frame within each swath contains identifiable landmarks. Through point-by-point comparison with maps and digital coastline data (CIA World Data Bank 2), a geolocation correction can be approximated for the entire path. After application of this procedure, root-mean-square (RMS) differences between control point locations on imagery and maps amounted to 1.5 km can be attributed to the inaccuracy of map data in these northern areas. This is acceptable considering the low resolution of the corresponding passive microwave data. Transparencies were digitized using a high resolution scanner, geolocated using the above outlined procedure, and projected to a polar stereographic projection (True at 70° latitude) used for the SSM/I gridded sea ice products.

Sensor Noise Removal. Landsat MSS image reflectance values are very low due to the low illumination conditions during spring and fall in the Arctic. Despite the high albedo of sea ice surfaces, digital images (CCT) frequently display maximum digital numbers (DN) not exceeding 40. Signal-to-noise ratios therefore are enhanced and significant "stitching" interference patterns are noticeable on contrast stretched digital imagery and photographic film products (Miller, 1986). A fast fourier transform (FFT) filter was used to remove sensor noise. Figure 1 (left) shows a subscene of a Landsat image with sensor noise, and Figure 1 (right) shows the same subscene after the FFT filter techniques were applied. Figure 2 depicts the power spectrum of the fast fourier transform from image 1 (left) and was used to identify the spatial frequencies of the noise pattern noticeable as a series of bright spots at higher spatial frequencies. The above described filtering scheme substantially reduced the amount of noise in the imagery and made the imagery more suitable for classification and extraction of sea ice concentrations.

Effects of varying solar zenith angles on Landsat imagery. During the process of classification of the Landsat MSS imagery, low frequency brightness variations or a darkening from one side of the image to the other, were discovered on many of the photographic Landsat images. These brightness variations seem to be unrelated to ice type variations or cloud interference but seemed to consistently occur along an axis in the direction of the sun. The brightness variation was strong enough to influence the result of the brightness threshold based sea ice type classification scheme. Figure 3 shows the relationship between the variation of solar elevation above horizon across the image, and the mean DN values (only values above DN = 100 were sampled). Despite the small solar elevation changes of only 2.3 degrees, a substantial change in mean DN values can be observed. Snow and ice surfaces display strong forward scattering characteristics at low sun angles (Steffen, 1987; Taylor and Stowe, 1984), thereby reducing the radiance in the direction of a near nadir satellite. In light of previous research, the magnitude of the solar zenith angle dependance is surprising. Nonlinearities during the film recording and digitization processes preclude an absolute calibration of DN values to radiances for the redigitized products. Digitally acquired (CCT) images used in this study did not display this feature because they originated from areas with greater solar elevations. To reduce this effect for the purpose of ice classification, images displaying a large brightness variation due to the solar zenith effect are corrected using a linear fit of observed mean brightness values to the solar elevation.

Ice classification. The MSS channel 7 is most useful for the determination of ice concentration because it displays the greatest reflectance differences between thin ice types and open water. The capability to distinguish thin ice types seems crucial for the validation of the SSM/I sea ice parameters because sea ice concentrations derived from passive microwave data are too low in the presence of thin ice (Steffen and Maslanik, 1988). For the ice type classification, two methods were developed.

Threshold techniques. Using training areas, the brightness value ranges for different ice types and open water are determined. By selecting appropriate brightness thresholds, an image can be classified into five different ice types (Plate 1). For the determination of ice concentration, the class spectrum comprised open water/dark nilas, light nilas, grey ice, grey-white ice, and white ice, corresponding to a categorization of ice thickness and stages of development commonly used in sea ice research (Steffen, 1986). During spring when only open water and white ice are present, a "subresolution" class was introduced. Pixels at intensity levels between open water and white ice where interpreted as containing ice floes of subresolution sizes and put into this class (Plate 2). Following classification, ice concentrations are calculated for the corresponding SSM/I 25- by 25-km and 50- by 50-km grid boxes.

Tie point algorithm. The algorithm procedure for sea ice concentration calculation from Landsat imagery developed by Comiso and Zwally (1982), is based on the idea that, during periods where no new ice formation occurs, the spectrum of classes is reduced to open water and white ice. If open water and white ice are the only two classes that are present, the

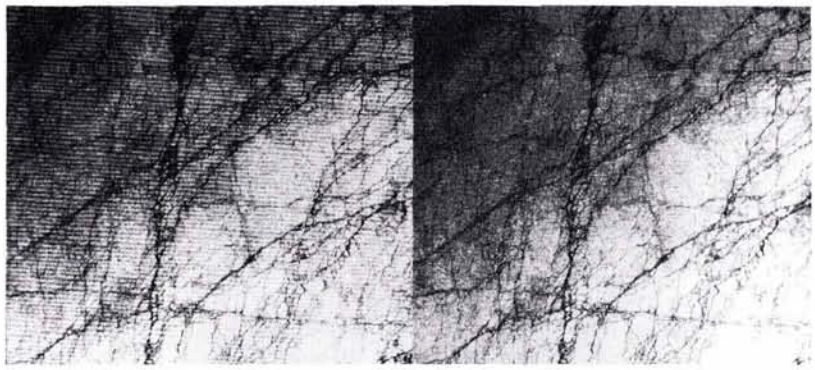

FIG. 1. Subscene of Landsat image. Left half of the image shows the striping pattern. Right half shows the same scene after the fast fourier transform filter technique has been applied.

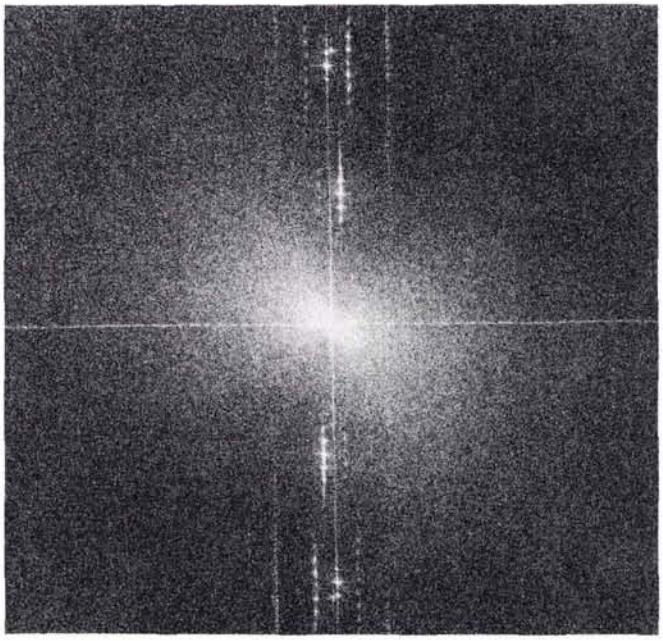

FIG. 2. Power spectrum of Landsat image shown in Figure 1. Spatial frequencies increase from 0 to 0.5 cycles/pix from the center of the spectrum towards the edges. The series of bright spots at higher spatial frequencies along the vertical axis represent the "stitching" pattern.

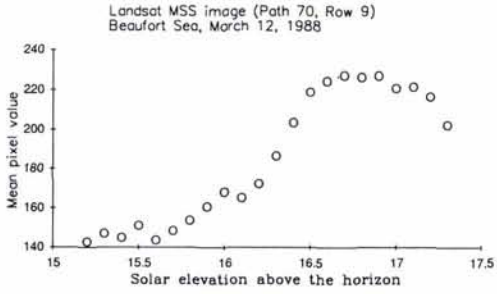

FIG. 3. Mean digital number (DN) values of homogeneous white ice for a Landsat image versus solar elevation.

assumption can be made that all brightness values in between those classes must represent ice concentrations at sub-resolution. Locations where a known state is assumed (i.e., 100 percent ice, 100 percent open water) are known as tie points. This algorithm thus more realistically accounts for the presence of ice floes smaller that the MSS resolution. The ice concentration (Ic) is determined from

$$Ic = ((D_x - D_l)/(D_h - D_l)) \times 100 \quad (1)$$

where

D_x = brightness value representing ice concentration,
D_l = brightness value for open water, and
D_h = brightness value for white ice.

Tie points were found using training areas for open water and large white ice floes, where D_h represents the mean brightness for that floe minus one standard deviation. Figure 4 shows a comparison of the tie point versus the threshold algorithm for grid cells of 5 by 5 km for a Landsat MSS image in the Weddell Sea. The tie point algorithm produces a more realistic distribution of ice concentrations with a histogram peak at *ca.* 90 percent rather than the near 100 percent peak produced by the threshold algorithm. Its attempt to account for sub-resolution size ice floes is physically more sound in areas where white ice and open water are the only surface types present. This was also found by Comiso and Zwally (1982) in comparing sea ice concentrations derived from the Electrical Scanning Microwave Radiometer (ESMR). In the subsequent analysis the tie point algorithm was used to calculate ice concentrations for images during spring conditions, when open water/black nilas and white ice where the only present surface classes. For other images, the threshold algorithm was applied.

AVHHR

AVHRR local area coverage (LAC) and High Resolution Picture Transmission (HRPT) images were obtained and registered to a polar stereographic projection for comparison with SSM/I and Landsat data. The tie point ice concentration algorithm developed for Landsat imagery was applied to the AVHRR data. So far no direct comparison of ice concentrations from AVHRR and Landsat data in the visible channels has been carried out. An initial comparison between ice concentrations derived from thermal AVHRR (Band 4, 10.3 to 11.3 μm) and Landsat (Band 7, 0.8 to 1.1 μm) imagery produced substantially lower ice concentrations for the AVHRR derived ice concentration products. It is assumed that this is caused by discrepancies between the thermal and reflective properties of thinner ice types. Therefore, thermal AVHRR imagery is not used in the comparisons presented here. However, it is one of the goals of the ongoing validation efforts to produce an intercomparison of ice retrieval capacities between different sensors.

SSM/I

Passive microwave data used in this study were acquired by the DMSP Special Sensor Microwave Imager (SSM/I). The instrument operates at four frequencies: 19.3, 22.2, 37.0, and 85.5 GHz. Vertical and horizontal polarizations are provided for each frequency, except for the 22.2 GHz channel. The effective field of view dimensions for the 19 and 37 Ghz radiometers used for ice concentration retrieval are 69 by 43 km and 37 by 28 km, respectively (along-track by cross-track). The 19 GHz and 37 Ghz channels are sampled to 25 to 25 km ground distance pixels corresponding to the Nyquist sampling rate of the 19 GHz channels. SSM/I orbital data were supplied by NASA Ocean Data System (NODS) and National Snow and Ice Data Center (NSIDC).

To investigate the effects of the undersampling of the 37 GHz channel, brightness temperatures were gridded to a 25-km grid, and a 50-km grid was produced by averaging four adjacent pixels. (A polar stereographic projection true at 70° latitude was used for both grids.) The calculation of a 50-km average grid corresponds to the specifications for the ice concentration product that will later be available through NSIDC (Weaver *et al.*, 1987) and represent an efficient alternative to a systematic smoothing of the 37 Ghz channel.

Ice Classification. Mapping of sea ice parameters using passive microwave data is possible owing to the large difference in emissivity between calm water and sea ice. In addition, the differences in emissivity of first-year versus old ice (sea ice that has survived at least one melt season) at different microwave frequencies provide a means of separating ice types. The capabilities of passive microwave data in sea ice research have been discussed in a number of articles (Svendsen *et al.*, 1983; Comiso, 1983, 1986; Cavalieri *et al.*, 1984; Gloersen and Cavalieri, 1986). The derivation of ice concentrations from the SSM/I data was carried out using the algorithm described by Cavalieri *et al.* (1984), with the addition of the weather filter as discussed by Gloersen and Cavalieri (1986).

The measured brightness temperatures of the 19 GHz vertical

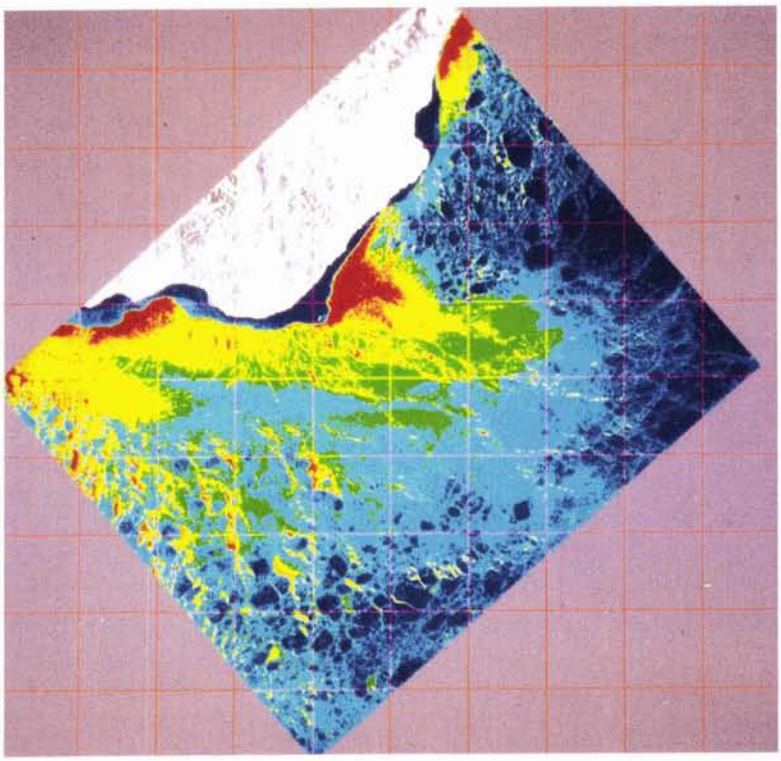

PLATE 1. Landsat image for the Bering Sea, south of Nome, Alaska. Ice types were classified with the threshold algorithm. The yellow grid depicts the position of the SSM/I grid cells (25 by 25 km). Red: open water; yellow: nilas; green: grey ice; light blue: grey-white ice; dark blue: white ice.

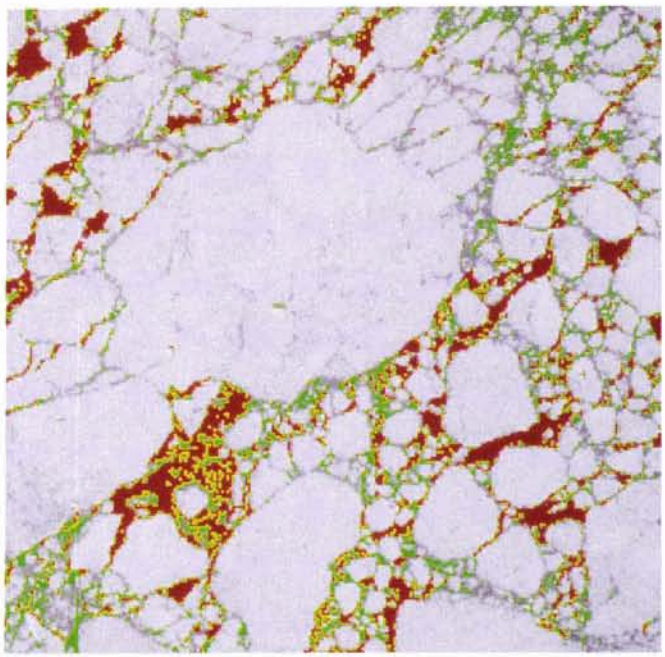

PLATE 2. Ice classification with threshold algorithm for a subscene of a Landsat MSS image. White areas depict ice, red areas open water, and green areas unresolved ice/open water mixture areas. The blue grid depicts the position of the SSM/I grid cells (25 by 25 km).

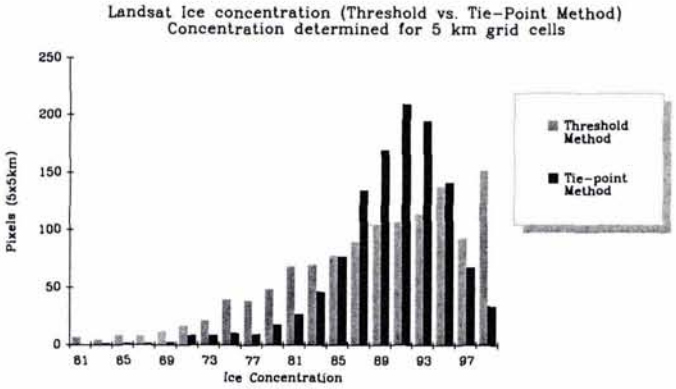

FIG. 4. Comparison of tie point versus threshold ice concentration algorithms for a Landsat image in the Weddell Sea.

and horizontal as well as the 37 GHz vertical channels are interpreted as the respective contributions of open ocean, first-year and multi-year ice, i.e.,

$$\mathrm{TB} = T_{BW}(1-C_f-C_m)+T_{BF}{}^{*}\,C_f+T_{BM}{}^{*}C_m \qquad (2)$$

where

T_{BW} is the:	brightness temperature of open water,
T_{BF} is the:	brightness temperature of first-year ice,
T_{BM} is the:	brightness temperature of multi-year ice,
C_f is the:	first-year ice concentration, and
C_m is the:	multi-year ice concentration.

The respective concentrations of multi- and first-year ice can then be expressed as a function of the polarization (PR) and gradient (GR) ratios and constant empirically determined brightness temperatures for open water, 100 percent first-year ice, and 100 percent multi-year ice. The gradient ratio is defined as the normalized difference between 37 GHz and 19 GHz brightness temperatures (Equation 6) and the polarization ratio represents the normalized difference of the 19 GHz vertical and horizontal polarizations (Equation 5). Constant brightness temperatures for open water, first-year ice, and multi-year ice are referred to as "tie points" owing to their function to implement real world boundary conditions on the algorithm

$$C_m = M_0 + M_1\mathrm{PR} + M_2\mathrm{GR} + M_3(\mathrm{PR})(\mathrm{GR}) \qquad (3)$$

$$C_f = F_0 + F_1\mathrm{PR} + F_2\mathrm{PR} + F_3(\mathrm{GR})(\mathrm{PR}) \qquad (4)$$

$$\mathrm{PR} = (T_{BV}(19)\text{-}T_{BH}(19))/(T_{BV}(19)+T_{BH}(19)) \qquad (5)$$

$$\mathrm{GR} = (T_{BV}(37)\text{-}T_{BV}(19))/(T_{BV}(37)+T_{BV}(19)) \qquad (6)$$

where

T_{BV}	=	vertically polarized brightness temperature,
T_{BH}	=	horizontally polarized brightness temperatures, and
$M_0,M_1,M_2,M_3,F_1,F_2,F_3$	=	constants dependent on tie points.

A graphical depiction of the algorithm is shown in Figure 5.

Tie points are brightness temperature values of open water (T_{BW}), first-year ice (T_{BF}), and multi-year ice (T_{BM}) as observed by the satellite, including atmosphere effects, and are critical for the accurate performance of the ice concentration retrieval algorithm. They are empirically determined based on statistics of hemispheric brightness temperatures (Cavalieri and Gloersen, 1984). If such "globally" chosen tie points are used for the calculation of ice concentration and multi-year ice fraction, the variation of T_{BW}, T_{BF}, and T_{BM} over time and space are ignored. However, there are large variations in T_{BW} along the ice edge, and in open and very open pack ice areas, caused by various effects including surface roughness, foam, and atmospheric water vapor content. A combination of these tends to increase the brightness temperature of the ocean by as much as 40 K. Also, T_{BF} are affected by spatial and temporal variations in physical temperature (Steffen and Maslanik, 1988), characteristics of emitting surface, and atmospheric conditions. Locally derived tie points were therefore used in this study using the following procedure. At least ten 25 by 25-km grid cells of open water were averaged near the ice edge over one to three days and used as water tie point (T_{BW}). To select tie points (T_{BF}), the highest brightness temperature values for the two frequencies and two polarizations were chosen for a larger geographic region (e.g., Beaufort Sea). For the selection of tie points representative of multi-year ice (T_{BM}), some local knowledge of the area is necessary as multi-year ice is not always found in the marginal seas. It is best to select an area in the Arctic Ocean north of 80° and choose the region with the lowest brightness temperature values. In order to locate areas of first-year ice and multi-year ice, SSM/I brightness temperatures were displayed using the SSM/I image display software which was developed for this purpose.

Ice concentrations were then calculated with the above described NASA-team algorithm using "local" tie points determined with the above described procedure. Tie points used for the individual case studies are listed in Table 1.

RESULTS

SSM/I derived ice concentrations based on global tie point statistics are compared with average AVHRR derived ice concentration for 25- by 25-km size pixels for an area in the East Greenland Sea (Figure 6). The SSM/I ice concentration algorithm overestimates ice concentration on average by 9.6 percent due to the global selection of tie points for this area. Individual pixels show substantially larger differences, with an extreme value of 42 percent. These large discrepancies are due to the undersampling of the 37 GHz channels and occur in areas of large brightness temperature contrast such as the ice edge. They are substantially reduced on the 50 km average grid that displays a mean error of 7.6 percent with maximal differences in ice concentrations of 24 percent.

In light of the fact that this particular case study reflects the more complicated summer situation with potential melt-freeze on top of the ice, these results must be viewed as reasonable. The application of locally adjusted tie points in this particular area, though difficult due to the lack of 100 percent first-year and multi-year ice areas, might further improve the results.

Effects due to wind or intense cloud systems can substantially alter the brightness temperatures over open ocean. Figure 7 shows a scatterplot of gradient (GR) versus polarization (PR) ratios (Equations 5 and 6) for manually classified ice covered (any concentration) areas and areas displaying intensive cloud cover due to a storm system moving through the area. The clear distinction between the cloud and ice clusters allows the filtering of weather contaminated pixels though the application of a gradient threshold at 0.05. Without application of this weather filter, ice concentrations of up to 18 percent would have been calculated for ice free areas in this particular image.

COMPARISON OF LANDSAT AND SSM/I DATA

The analysis was carried out for two different grid sizes, 25 by 25 km and 50 by 50 km, of which the 50 km grid is defined as a standard for SSM/I ice concentration products.

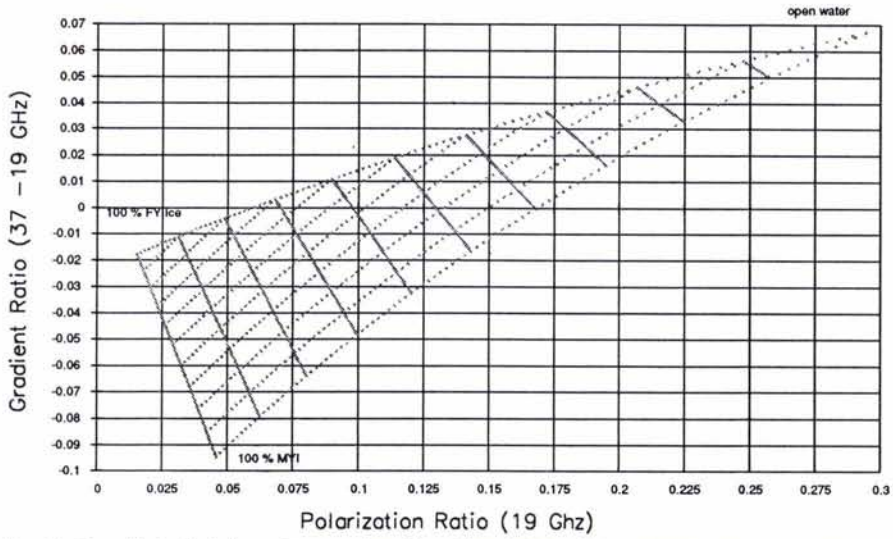

FIG. 5. Graphical depiction of SSM/I algorithm. The inside of the triangle describes total ice concentrations from 0 to 100 percent along the longer sides of the triangle and multi-year ice fractions along the shorter side. The corners of the triangle represent tie points for open water, 100 percent first year ice, and 100 percent multi-year ice. (After Cavalieri and Gloersen, 1986).

TABLE 1. SSM/I TIE POINTS UTILIZED IN THE PRESENTED CASE STUDIES. COLUMNS SHOW DATE OF CASE STUDY ALONG WITH TB VALUES FOR OPEN OCEAN (OW), FIRST-YEAR ICE (FY), AND MULTI-YEAR ICE (MY) FOR THE DIFFERENT FREQUENCIES (19,37) AND POLARIZATIONS (V, H).

Date	$19V_{OW}$	$19H_{OW}$	$19V_{FY}$	$19H_{FY}$	$19V_{MY}$	$19H_{MY}$	$37V_{OW}$	$37V_{FY}$	$37V_{MY}$
87-09-17	187	120	245	230	222	202	209	245	184
87-11-10	185	115	252	232	222	202	205	250	184
88-03-12	177	100	258	241	228	204	200	255	196

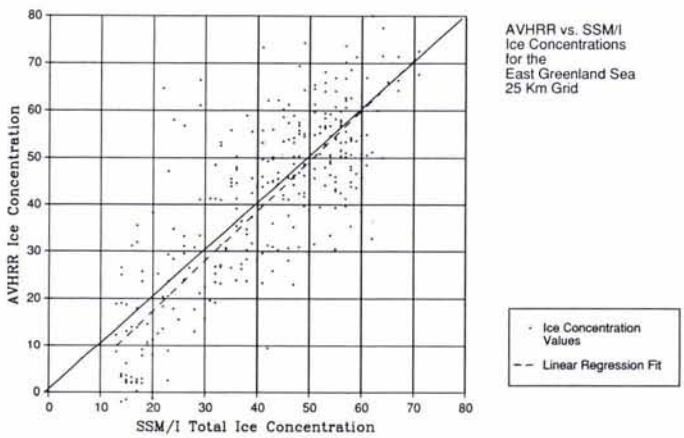

FIG. 6. Comparison SSM/I versus AVHRR derived ice concentrations for East Greenland Sea area. AVHRR ice concentrations are averaged for 25- by 25-km grid cells. Weather contaminated pixels have been removed.

Three different ice conditions were analyzed for the Beaufort Sea region, covering an ice concentration range from 0 to 100 percent: (1) very open pack ice before freeze-up, (2) close pack ice during freeze-up, and (3) very close pack ice during spring (premelt). The results of the Landsat-SSM/I ice concentration comparison for the two different grids sizes are summarized in Table 2.

The first case study 19 Sept. 1988) represents the very open pack ice situation (mean ice concentration of 13 percent) along the ice edge with air temperatures above freezing. For 50- by 50-km grid cells a mean difference between Landsat and SSM/I ice concentration of 2.7 percent was found with a maximum value of 5.9 percent. For 25-km grid cells the mean difference was 4.8 percent with a maximum value of 23.4 percent. This increase in difference between 50-km and 25-km grid cells is mainly due to the undersampling of the 37 GHz channel. Therefore, brightness temperature values averaged to 50 by 50 km reveal better accuracies for ice concentration. In addition, there is always a difference in data acquisition time between Landsat and SSM/I satellites which accounts for some ice concentration differences, mainly in areas of low ice concentrations. In the Beaufort Sea area the time lage between the two satellites was 6 hours.

The freeze-up situation in the Beaufort Sea is shown in the next case study (10 Nov. 1987) with Landsat ice condition values between 91 and 97 percent. The following ice types were classified from the two Landsat images: 5.9 percent open water and dark nilas, 5.1 percent grey ice, 38.3 percent grey-white ice, and 50.3 percent white ice. For 50- by 50-km grid cells, Landsat and SSM/I ice concentrations give a mean difference of 4.3 percent, with a maximum value of 9.7 percent. This large difference—even with locally chosen tie points—reveals some limitation of the NASA-team algorithm under freeze-up condition (extensive young ice areas). Work on that problem is in progress.

The very close pack ice situation is shown in the third case study (12 March 1988) in spring with ice concentrations above 95 percent (Table 2). The mean difference between Landsat and SSM/I ice concentrations is less than 1 percent with a maximum value of 1.7 percent.

CONCLUSIONS

The data set of SSM/I, Landsat, and AVHRR imagery serves as an excellent tool for evaluating the ice parameter retrieval capabilities of the SSM/I passive microwave sensor. The influence of smaller scale features, such as ice types and stage of development on the low resolution passive microwave sensor, is best addressed through a comparison with Landsat MSS imagery at 80-m resolution. Larger scale features such as ice edge position and weather effects necessitate a synoptic overview provided

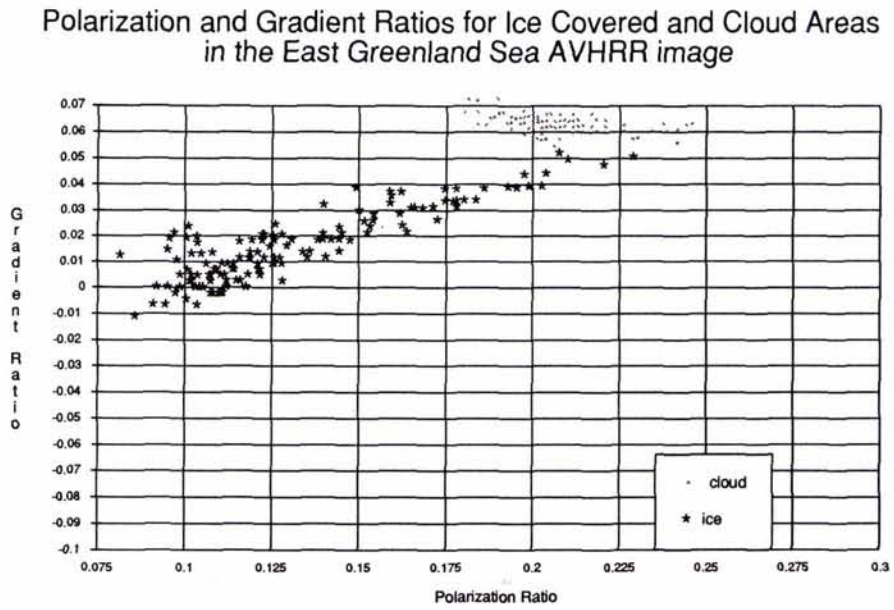

FIG. 7. Scatterplot of *Gradient Ratio versus Polarization Ratio for East Greenland Sea area.* Manually interpreted ice and cloud over open ocean areas are shown in different symbols. Note the clear definition of the ice versus the cloud clusters that allows the application of a gradient threshold of 0.05.

TABLE 2. DIFFERENCES BETWEEN LANDSAT ICE CONCENTRATION AND SSM/I ICE CONCENTRATION FOR THE BEAUFORT SEA REGION FOR THREE DIFFERENT CASE STUDIES: (1)19 SEPT. 1987, VERY OPEN PACK ICE BEFORE FREEZE-UP; (2) 10 NOV. 1987, CLOSE PACK ICE DURING FREEZE-UP; AND (3) 12 MARCH 1988, VERY CLOSE PACK ICE DURING SPRING. THE MIN AND MAX REPRESENT THE SMALLEST AND LARGEST DIFFERENCES IN ICE CONCENTRATION FOR AN INDIVIDUAL CASE STUDY. THE LAST COLUMN REPRESENTS AN ESTIMATE OF THE 95 PERCENT CONFIDENCE INTERVAL FOR THE POPULATION MEAN ERROR BASED ON T-STATISTICS.

Date	Grid	Mean	Std Dev	Min	Max	#cells	Conf.Int
87-09-17	50 km	2.7	2.7	0.2	5.9	9	+/−2.0
87-11-10	50 km	4.3	2.9	1.6	9.7	6	+/−2.9
88-03-12	50 km	0.8	0.7	0.1	1.7	7	+/−0.6
87-09-17	25 km	4.8	5.8	0.0	23.4	47	+/−0.2
87-11-10	25 km	6.1	4.0	0.0	12.9	36	+/−1.3
88-03-12	25 km	1.1	1.0	0.0	4.6	51	+/−0.2

by AVHRR imagery at the 1-km resolution. This approach of an investigation at different levels of spatial integration is important for the establishment of reliable data retrieval procedures as well as the documentation of potential errors.

The average retrieval errors of the SSM/I algorithm, ranging between 1.7 percent for spring conditions and 4.3 percent during freeze up in comparison with Landsat derived ice conditions, are excellent considering the level of spatial integration of the SSM/I sensor, and we recommend this retrieval procedure for the development of a long term database for large-scale applications. While extreme errors for individual pixels are substantially larger (up to 9.7 percent for freeze up conditions using the 50-km grid), the potential applications of passive microwave derived ice concentration data will be primarily large scale and more focused on average trends rather than on ice concentrations within individual footprints.

The achieved accuracy of the SSM/I algorithm in the presented case studies is in part due to the application of locally selected tie points that account for the spatial and temporal variations of ice type and surface roughness. For the calculation of hemispheric ice concentrations, two approaches may be taken. One is to derive a "global" tie point set that ignores the seasonal and geographic variability of ice types and atmospheric conditions and therefore achieve a somewhat lower accuracy. Alternatively, statistics on the seasonal and geographic distribution of ice and atmospheric parameters, as reflected in the variability of brightness temperatures, could form the bases for the selection of "regional and seasonal" tie points. While further work is needed to investigate the applicability of a such a tie point database on a hemispheric scale, local tie points can certainly increase the retrieval accuracy for regional scale studies.

ACKNOWLEDGMENTS

This research was funded by NASA Ocean Sciences Branch under contract NAG 5-882 to K. Steffen and R.G. Barry. Additional support is provided by the Swiss Federal Institute of Technology. Thanks are due to Ron Weaver and Roger Barry of NSIDC for their scientific inputs as well as administrative assistance. Don Cavalieri's suggestions as well as Bob Thomas's encouragement were invaluable in this research. Charles Morris at NODS and Frank Wentz at Remote Sensing Systems provided SSM/I data. Vince Troisi was most helpful in overcoming many of the computational problems. Bill Emery and Molly McElroy of CCAR provided AVHRR data and navigation software. Staff at the Landsat Quick-Look Facility operated by the University of Alaska provided imagery. Thanks are also due to the IBM Corporation for providing the scientific community with its international BITNET network. Without it, this project involving institutions on both sides of the Atlantic Ocean would have been impossible.

REFERENCES

Cavalieri, D. J., P. Gloersen, and W. J. Campbell, 1984. Determination of sea ice parameters with Nimbus 7 SMMR, *J. Geophys. Res.*, 89, pp. 5355–5369.

Comiso, J. C., 1983. Sea ice effective microwave emissivities from sat-

ellite passive microwave and infrared observations, *J. Geophys. Res.*, 88(C12), pp. 7686–7704.

———, 1986. Characteristics of arctic winter sea ice from satellite multispectral microwave observations, *J. Geophys. Res.*, 91(C1), pp. 975–994.

Comiso, J. C., and H. J. Zwally, 1982. Antarctic sea ice concentrations inferred from Nimbus 5 ESMR and Landsat Imagery, *J. Geophys. Res.*, 87(C8), pp. 5836–5844.

Gloersen, P., and D. J. Cavalieri, 1986. Reduction of weather effects in the calculation of sea ice concentration from microwave radiances, *J. Geophys. Res.*, 91(C3), pp. 3913–3919.

Hansen, J., I. Fung, A. Lacis, D. Rind, S. Lebedeff, R. Ruedy, G. Russell, and R. Stone, 1988. Global climate changes as forecasted by Goddard Institute for Space Studies three-dimensional model, *J. Geophys. Res.* 93(D8), pp. 9341–9364.

Miller, J. M., N. Campbell, and R. Mackinnon, 1981. An Experimental Landsat Quick-Look System for Alaska. *Proc. Seventh International Symposium on Machine Processing of Remotely Sensed Data*, pp. 639–646.

Miller, J. M., G. B. Berger, 1986. Enhancing Landsat Data acquired under very low illumination. *Photogrammetric Engineering and Remote Sensing*, Vol. 52, No. 6, June 1986, pp. 801–807.

Steffen, K., 1986. *Atlas of sea ice types, deformation processes and openings in the ice*, Zürcher Geographische Schriften, 20, Swiss Federal Institute of Technology, Zürich, Switzerland, 55p.

———, 1987. Bidirectional reflectance of snow at 500–600 nm, Large Scale Effects of Seasonal Snow Cover, *IAHS Publ.* 166, pp. 415–425.

Steffen, K., and J. A. Maslanik, 1988. Comparison of Nimbus 7 scanning multichannel radiometer radiance and derived sea ice concentrations with Landsat imagery for the North Water area of Baffin Bay, *J. Geophys. Res.*, 93(C9), pp. 10,769–10781.

Svendsen, E., K. Kloster, B. Farrelly, O. M. Johannessen, H. A. Johannessen, W. J. Campbell, P. Gloersen, D. J. Cavalieri, and C. Matzler, 1983. Norwegian remote sening experiment: Evaluation of the Nimbus-7 scanning multichannel microwave radiometer for sea ice research, *J. Geophys. Res.*, 88(C5), pp. 2781–2791.

Taylor, V. R., and L. L. Stowe, 1984. Reflectance characteristics of uniform earth and cloud surfaces derived from Nimbus 7 ERB, *J. Geophys. Res.*, 89(D4), pp. 4987–4996.

Weaver, R., C. Morris, and R. G. Barry, 1987. Passive microwave data for snow and ice research: planned products from the DMSP SSM/I system, *EOS*, 68(39), pp. 776–777.